INTERNATIONAL JOURNAL FOR NUMERICAL METHODS IN FLUIDS, VOL. 8, 845–861 (1988)

COMPARISON OF TWO NUMERICAL METHODS FOR THE SOLUTION OF NON-NEWTONIAN FLOW IN DUCTS

TA-JO LIU, HO-MAY LIN AND CHIN-NAN HONG

Department of Chemical Engineering, National Tsing Hua University, Hsinchu, Taiwan 30043, Republic of China

SUMMARY

Two numerical methods, the Galerkin finite element method (FEM) and the boundary-fitted co-ordinate transformation method (BFCTM), have been applied to solve inelastic non-Newtonian fluid flow in ducts of irregular cross-section. Three representative fluid models, namely the power-law, the Ellis and the Bingham models, have been analysed. The application of the FEM is straightforward, while for the BFCTM the accurate estimation of viscosity on the duct boundary and the proper mesh adjustment appear to be critical for generating convergent solutions. A detailed comparison of the two numerical methods in terms of volumetric flow rate, axial velocity, shear rate, viscosity and CPU time is given. Both methods can generate accurate solutions of velocity over a wide range of variables, but the FEM requires much less computing time to reach the same level of accuracy. Only the BFCTM can be used to approximate shear rate and viscosity with reasonable accuracy.

KEY WORDS Non-Newtonian flow FEM vs FDM Duct flow

INTRODUCTION

Ducts of irregular cross-section appear in many industrial applications.[1] The motion of inelastic non-Newtonian fluids in ducts has been analysed by many authors. The information obtained, particularly the pressure drop/flow rate equation, is quite useful for practical engineering needs. Existing technical articles for estimating the pressure drop/flow rate equation for non-Newtonian fluids in ducts can be divided into two categories: theoretical and empirical. For the theoretical part, the equations of motion have to be solved first to obtain the velocity distribution and then an integration is performed to determine the pressure drop/flow rate equation. Previous authors used the variational principle,[2-5] the finite difference method[6] and the finite element method.[7] All the authors assumed that the fluid under consideration obeyed the popular non-Newtonian power-law model, except Reference 5. For the empirical part, Kozicki *et al.*[8] and Miller[1] proposed some simple methods; however, the ranges of applicability and the accuracy of their methods need to be examined carefully.[9, 10]

Mathematically speaking, there are two difficulties in solving the duct flow problem, namely the duct geometry may be quite irregular and the constitutive equations of non-Newtonian fluids are rather complicated, which will create a highly non-linear mathematical problem. Currently there are two numerical methods that can be used effectively to treat the irregular domain of integration: the finite element method (FEM) and the boundary-fitted co-ordinate transformation method (BFCTM). Both methods can be combined with conventional iterative techniques to solve non-linear problems. The FEM appears to be more popular for non-Newtonian flow problems.

0271–2091/88/070845–17$08.50

Received 24 June 1987
Revised 21 September 1987

In this paper we shall present the results of applying these two numerical methods for solving the duct flow problem. In addition to the power-law model, we have extended our analysis to more realistic generalized Newtonian fluid (GNF) models. Although the methods are applicable to any GNF models, we only consider the power-law, the Ellis and the Bingham models here. Three duct geometries were studied: circular, square and equilateral triangular. The computational results were examined in terms of velocities, volumetric flow rates, shear rates and viscosities. The CPU time consumed and the ranges of convergence for this highly non-linear mathematical problem are also discussed. Since the exact solutions are available for fluid flow of these three models in a circular duct, our comparison will emphasize this duct geometry.

MATHEMATICAL FORMULATION

The flow geometry is shown in Figure 1. We consider isothermal, incompressible and fully developed laminar flow of non-Newtonian fluids driven by a constant pressure gradient in a duct of arbitrary cross-section. The cross-sectional area of the duct remains constant in the $\bar{z}$-direction. Since secondary flows are weak and have negligible effect on the pressure drop/flow rate equation,[11] we assume that the velocity is purely axial and $\bar{w}$ is the only non-vanishing velocity component. The equations of motion reduce to a single equation:[7]

$$\frac{\partial}{\partial \bar{x}}(\bar{\tau}_{xz})+\frac{\partial}{\partial \bar{y}}(\bar{\tau}_{yz})=-\frac{\mathrm{d}\bar{P}}{\mathrm{d}\bar{z}}=\text{constant} \quad \text{in} \quad \bar{D}. \tag{1}$$

The constitutive equation for the GNF models can be represented as[11]

$$\boldsymbol{\tau}=-\bar{\eta}\boldsymbol{\Delta} \tag{2}$$

and the non-Newtonian viscosity may depend on the scalar invariants of the tensor $\boldsymbol{\tau}$ or $\boldsymbol{\Delta}$. $\bar{\tau}_{xz}$ and $\bar{\tau}_{yz}$ are given by

$$\bar{\tau}_{xz}=-\bar{\eta}(\partial\bar{w}/\partial\bar{x}), \tag{3a}$$

$$\bar{\tau}_{yz}=-\bar{\eta}(\partial\bar{w}/\partial\bar{y}). \tag{3b}$$

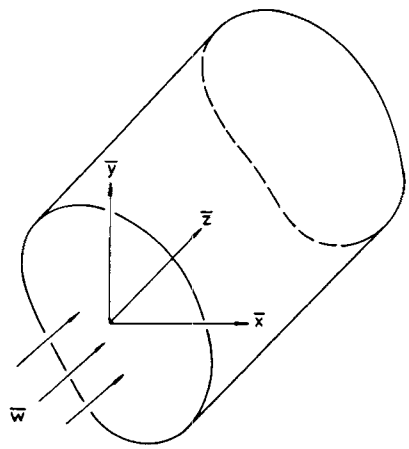

Figure 1. Flow geometry

Substituting (3) into (1), we obtain

$$\frac{\partial}{\partial \bar{x}}\left(\bar{\eta}\frac{\partial \bar{w}}{\partial \bar{x}}\right)+\frac{\partial}{\partial \bar{y}}\left(\bar{\eta}\frac{\partial \bar{w}}{\partial \bar{y}}\right)=\frac{\mathrm{d}\bar{P}}{\mathrm{d}\bar{z}} \quad \text{in} \quad \bar{D}. \tag{4}$$

We consider three representative GNF models here and $\bar{\eta}$ can be presented as:

The power-law model

$$\bar{\eta}_{\mathrm{P}}=k\left[\left(\frac{\partial \bar{w}}{\partial \bar{x}}\right)^2+\left(\frac{\partial \bar{w}}{\partial \bar{y}}\right)^2\right]^{(n-1)/2}. \tag{5}$$

The Ellis model

$$\frac{\eta_0}{\bar{\eta}_{\mathrm{E}}}=1+\left(\frac{(\bar{\tau}_{xz}^2+\bar{\tau}_{yz}^2)^{1/2}}{\tau_{1/2}}\right)^{\alpha-1}. \tag{6}$$

The Bingham model

$$\begin{aligned}&\bar{\eta}_{\mathrm{B}}=\infty, \quad \bar{\tau}\leqslant\tau_0,\\ &\bar{\eta}_{\mathrm{B}}=\eta_0+\tau_0\Big/\left[\left(\frac{\partial \bar{w}}{\partial \bar{x}}\right)^2+\left(\frac{\partial \bar{w}}{\partial \bar{y}}\right)^2\right]^{1/2}, \quad \bar{\tau}>\tau_0.\end{aligned} \tag{7}$$

The power-law and the Ellis models can represent fluids with shear-thinning behaviour, but the power-law model fails for the low-shear-rate region. The Bingham model describes a fluid with a yield stress.[11]

We define the dimensionless variables

$$\eta=\bar{\eta}/\eta_0, \qquad (x, y)=(\bar{x}, \bar{y})/h, \qquad w=\bar{w}\eta_0/h^2(-\mathrm{d}\bar{P}/\mathrm{d}\bar{z}), \tag{8}$$

with the characteristic length $h=\bar{D}/S$. The average wall stress τ_{w} is defined as

$$\tau_{\mathrm{w}}\equiv h(-\mathrm{d}\bar{P}/\mathrm{d}\bar{z}). \tag{9}$$

Substituting (8) and (9) into (4)–(7), we obtain

$$\frac{\partial}{\partial x}\left(\eta\frac{\partial w}{\partial x}\right)+\frac{\partial}{\partial y}\left(\eta\frac{\partial w}{\partial y}\right)=-1 \quad \text{in} \quad D \tag{10}$$

and the viscosity equations are

$$\eta_{\mathrm{P}}=\left[\left(\frac{\partial w}{\partial x}\right)^2+\left(\frac{\partial w}{\partial y}\right)^2\right]^{(n-1)/2}, \tag{11}$$

$$\eta_{\mathrm{E}}^{-1}=1+\left(\frac{\tau_{\mathrm{w}}}{\tau_{1/2}}\right)^{\alpha-1}\eta_{\mathrm{E}}^{\alpha-1}\left[\left(\frac{\partial w}{\partial x}\right)^2+\left(\frac{\partial w}{\partial y}\right)^2\right]^{(\alpha-1)/2}, \tag{12}$$

$$\begin{aligned}&\eta_{\mathrm{B}}=\infty, \quad \bar{\tau}\leqslant\tau_0,\\ &\eta_{\mathrm{B}}=1+\left(\frac{\tau_0}{\tau_{\mathrm{w}}}\right)\Big/\left[\left(\frac{\partial w}{\partial x}\right)^2+\left(\frac{\partial w}{\partial y}\right)^2\right]^{1/2}, \quad \bar{\tau}>\tau_0.\end{aligned} \tag{13}$$

Here we select η_0 for the power-law model as

$$\eta_0=k^{1/n}\tau_{\mathrm{w}}^{1-1/n}$$

and the shear rate γ is defined as

$$\gamma=\left[\left(\frac{\partial w}{\partial x}\right)^2+\left(\frac{\partial w}{\partial y}\right)^2\right]^{1/2}.$$

The no-slip boundary condition is

$$w=0 \quad \text{at} \quad \partial D. \tag{14}$$

The volumetric flow rate $\bar{V}$ is

$$\bar{V}=\int\int_{\bar{D}} \bar{w}\,\mathrm{d}\bar{x}\,\mathrm{d}\bar{y} \tag{15}$$

$$=\frac{h^3\tau_w}{\eta_0}\lambda, \tag{16}$$

where

$$\lambda=\int\int_{D} w\mathrm{d}x\,\mathrm{d}y$$

is the dimensionless volumetric flow rate.

For the power-law model we have

$$\bar{V}=\frac{h^3\tau_w^{1/n}}{k^{1/n}}\lambda. \tag{17}$$

We can solve (10)–(14) for w. Once w is available, we can perform a numerical integration to obtain λ and then the pressure drop/flow rate equation (16) or (17) is determined completely. Note that for the power-law model the formulation is independent of τ_w, and n is the only variable that needs to be specified in the computation. If we select $h=(\bar{D})^{1/2}$, this formulation is identical to the case of Reference 7.

NUMERICAL PROCEDURE

The finite element method

We use the Galerkin finite element method with an isoparametric element to solve the flow problem. w, x and y can be approximated as

$$\begin{bmatrix} w \\ x \\ y \end{bmatrix} = \sum_{i=1}^{L} \begin{bmatrix} w_i \\ x_i \\ y_i \end{bmatrix} \phi_i, \tag{18}$$

where L represents the number of nodes in each element and ϕ is the interpolation function.

We apply the Galerkin process to (10). After performing an integration by parts and incorporating boundary condition (14), we obtain

$$\delta_m(w)=K_{mi}w_i-A_m=0, \quad m, i=1, 2, \ldots, L, \tag{19}$$

where

$$K_{mi}=\iint_e \eta\beta_{mi}\mathrm{d}x\mathrm{d}y, \tag{20}$$

$$A_m=\iint_e \phi_m \mathrm{d}x\mathrm{d}y \tag{21}$$

and

$$\beta_{mi}=\frac{\partial\phi_m}{\partial x}\frac{\partial\phi_i}{\partial x}+\frac{\partial\phi_m}{\partial y}\frac{\partial\phi_i}{\partial y}, \tag{22}$$

with e the area of the element.

To evaluate (20)–(22), we transform e to a local co-ordinate system and then perform a numerical integration using the Gaussian quadrature method. We have used the nine-node Lagrangian element in our computation because it has been identified[12–14] as a powerful element for generating accurate numerical solutions. The 2×2 and 3×3 Gaussian quadrature methods were used for numerical integration and the Gauss points can be found in standard textbooks.[15, 16]

Equation (19) was previously solved for power-law fluids by the FEM.[7] The viscosity function (17) was substituted into (19) and then Newton's method was applied to determine w. However, this approach is not suitable for GNF models such as Ellis fluids; even if we introduce (12) into (19), the viscosity η_E cannot be eliminated and there are two unknowns, w and η_E, in the resulting equation.

The method suggested by Lyness *et al.*[17] was adopted for our computation. If we assume the values of η at the Gauss points, then K_{mi} and A_m can be evaluated easily and (19) reduces to a linear system of equations which can be solved by the frontal method.[18] With the values of w available, we can estimate the velocity gradients by differentiating the interpolation function for w in (18) and update the viscosities at the Gauss points. This iterative process can be repeated until convergence is achieved.

The above approach can be carried out straightforwardly for power-law fluids. The Ellis model gives an implicit relation between the viscosity and the velocity gradients as indicated in (12). An iterative scheme is needed to update the viscosity at the Gauss points and we used Newton's method in our computation. For the Bingham model the 'infinity' in (13) needs some modifications so that it is suitable for computation. We adopted the strategy of O'Donovan and Tanner[19] to approximate the Bingham model numerically, and (13) is modified as

$$\begin{aligned}&\eta_B=1000, \quad |\gamma|\leqslant\gamma_c,\\ &\eta_B=1+\left(\frac{\tau_0}{\tau_w}\right)\Big/\left[\left(\frac{\partial w}{\partial x}\right)^2+\left(\frac{\partial w}{\partial y}\right)^2\right]^{1/2}, \quad |\gamma|>\gamma_c,\end{aligned} \tag{23}$$

and $\tau_0=|\gamma_c|(\eta_B-1)=999|\gamma_c|$.

The number 1000 was selected arbitrarily. We found, as previous authors observed,[19] that as long as this number is large it will not affect the numerical solutions.

The finite difference method

The study of the numerical generation of the curvilinear co-ordinate system has been reviewed by Thompson *et al.*[20] The BFCTM developed by Thompson *et al.*[21] is used here to map the duct

geometry to a rectangular domain for numerical integration. Thompson's method requires us to solve the following two mapping equations:

$$ax_{\xi\xi}-2bx_{\xi\zeta}+cx_{\zeta\zeta}+J^2(Px_\xi+Qx_\zeta)=0, \tag{24a}$$

$$ay_{\xi\xi}-2by_{\xi\zeta}+cy_{\zeta\zeta}+J^2(Py_\xi+Qy_\zeta)=0, \tag{24b}$$

where

$$a=x_\xi^2+y_\xi^2, \quad b=x_\xi x_\zeta+y_\xi y_\zeta, \quad c=x_\zeta^2+y_\zeta^2, \quad J=x_\xi y_\zeta-x_\zeta y_\xi, \tag{24c}$$

and subscripts denote partial differentiation. The functions P and Q are used to regulate the mesh intervals.

Following Wheeler and Wissler,[6] we rearrange (10) to eliminate first-order derivatives. The resulting equation has the form

$$\nabla^2(\eta w)+\eta\nabla^2 w-w\nabla^2\eta+2=0 \quad \text{in} \quad D, \tag{25}$$

where ∇^2 is the Laplacian

$$\nabla^2=\partial^2/\partial x^2+\partial^2/\partial y^2. \tag{26}$$

Equation (25) is also transformed to (ξ, ζ) co-ordinates to give

$$\begin{aligned}[a(\eta w)_{\xi\xi}-2b(\eta w)_{\xi\zeta}+c(\eta w)_{\zeta\zeta}]/J^2+[P(\eta w)_\xi+Q(\eta w)_\zeta]\\ +\eta(aw_{\xi\xi}-2bw_{\xi\zeta}+cw_{\zeta\zeta})/J^2+\eta(Pw_\xi+Qw_\zeta)\\ -w(a\eta_{\xi\xi}-2b\eta_{\xi\zeta}+c\eta_{\zeta\zeta})/J^2-w(P\eta_\xi+Q\eta_\zeta)=-2.\end{aligned} \tag{27}$$

We use second-order formulae to discretize (24) and (27). The rectangular domain in (ξ, ζ) co-ordinates is divided into $M+1$ segments in the ξ-direction and $N+1$ segments in the ζ-direction. Hence $i=0, M+1$ correspond to the boundary line in the ξ-direction and $j=0, N+1$ correspond to the boundary line in the ζ-direction.

For a function $f(\xi, \zeta)$, its first and second derivatives can be approximated as

$$\begin{aligned}(f_\xi)_{i,j}&=(1/2r)(f_{i+1,j}-f_{i-1,j}),\\ (f_\zeta)_{i,j}&=(1/2s)(f_{i,j+1}-f_{i,j-1}),\\ (f_{\xi\xi})_{i,j}&=(1/r^2)(f_{i+1,j}-2f_{i,j}+f_{i-1,j}),\\ (f_{\zeta\zeta})_{i,j}&=(1/s^2)(f_{i,j+1}-2f_{i,j}+f_{i,j-1}),\\ (f_{\xi\zeta})_{i,j}&=(1/4rs)(f_{i+1,j+1}-f_{i+1,j-1}-f_{i-1,j+1}+f_{i-1,j-1}),\end{aligned} \tag{28}$$

where $r=\Delta\xi$, $s=\Delta\xi$, $\xi_i=ir$, $\zeta_j=js$ and $f_{i,j}$ stands for $f(\xi_i, \zeta_j)$.

Derivatives on the boundary can be approximated using one-sided formulae. We have used two sets of formulae:

One-sided formulae with second-order accuracy

$$\begin{aligned}(f_\xi)_{0,j}&=(1/2r)(-f_{2,j}+4f_{1,j}-3f_{0,j}),\\ (f_\zeta)_{i,0}&=(1/2s)(-f_{i,2}+4f_{i,1}-3f_{i,0}),\\ (f_\xi)_{M+1,j}&=(1/2r)(f_{M-1,j}-4f_{M,j}+3f_{M+1,j}),\\ (f_\zeta)_{i,N+1}&=(1/2s)(f_{i,N-1}-4f_{i,N}+3f_{i,N+1}).\end{aligned} \tag{29}$$

One-sided formulae with first-order accuracy

$$\begin{aligned}(f_\xi)_{0,j}&=(1/r)(f_{1,j}-f_{0,j}),\\(f_\zeta)_{i,0}&=(1/s)(f_{i,1}-f_{i,0}),\\(f_\xi)_{M+1,j}&=(1/r)(f_{M+1,j}-f_{M,j}),\\(f_\zeta)_{i,N+1}&=(1/s)(f_{i,N+1}-f_{i,N}).\end{aligned}\tag{30}$$

The mapping procedure follows the work of Thompson *et al.*[21] For a given duct geometry we first discretize the boundary and assign the corresponding mesh points on the boundary of the rectangle in the transformed plane; then we give guessed values of the interior mesh points (x, y) in the (ξ, ζ) plane. With these guessed values we can estimate a, b, c and J in (24c) using (28). After applying (28) to discretize (24a) and (24b), the resulting linear systems of equations are solved by the successive line over-relaxation method (SLOR). If the maximum difference between the newly generated values and the guessed values is larger than a preset tolerance, we will repeat the process. The numerical mapping is complete after the convergent solution is obtained. Values of a, b, c and J will be used in (27).

There are two unknowns, w and η, in (27). We first guess w; the velocity derivatives in the viscosity expressions (11)–(13) can then be approximated using (28) and either (29) or (30). With values of η available on all the mesh points in the (ξ, ζ) plane, we can solve (27) for w and again SLOR is used. We now check convergence for w; if the convergence criterion is not met, we replace the guessed values of w by the new values and repeat the process. We can either (i) update η each time with the newly generated w or (ii) keep η fixed until we obtain the convergent solution of w and then update η and repeat the process. We have found the second approach is more effective. The methods of updating the viscosities for the three fluid models are the same as those of the FEM, except that the values are computed at the mesh points.

RESULTS AND DISCUSSION

We have selected three representative duct geometries for our computation: circular, square and equilateral triangular. All the calculations were performed on a CDC Cyber 180/840 machine. The tolerance of convergence was fixed to be $1{\cdot}0 \times 10^{-5}$. Comparison of the two methods will be carried out in terms of w, λ, γ, η, the ranges of convergence and the CPU time consumed. Since the exact solutions are available for a circular duct, our comparison will emphasize this duct geometry. The results for the three fluid models will be discussed separately.

The power-law model

We started our analysis with a circular duct. Two grids were used for the FEM. The crude grid (grid F1) is shown in Figure 2 and consists of 12 elements and 57 nodes. The refined grid (grid F2) was obtained by dividing each of the interior elements into four equal elements and the boundary elements into two elements, as indicated by the broken lines in Figure 2, to give 32 elements and 147 nodes in grid F2. For the BFCTM we divided the boundary of the circular duct into equal segments and transformed the duct into a square in (ξ, ζ) co-ordinates. To simplify our computation, we selected $r=s$ and fixed the relaxation factor to be 1·75 for all the BFCTM computations. Three grids were used, with 10×10 (grid B1), 20×20 (grid B2) and 30×30 (grid B3) points. Grid B2 is shown in Figure 3.

The iterative method (Picard method) we used for the FEM is quite effective for power-law

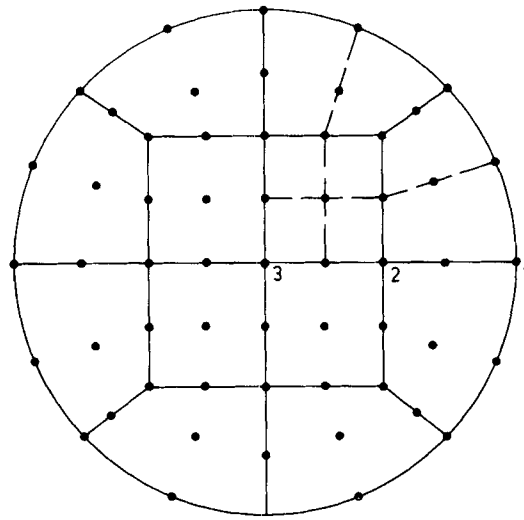

Figure 2. Grid F1 for the FFM

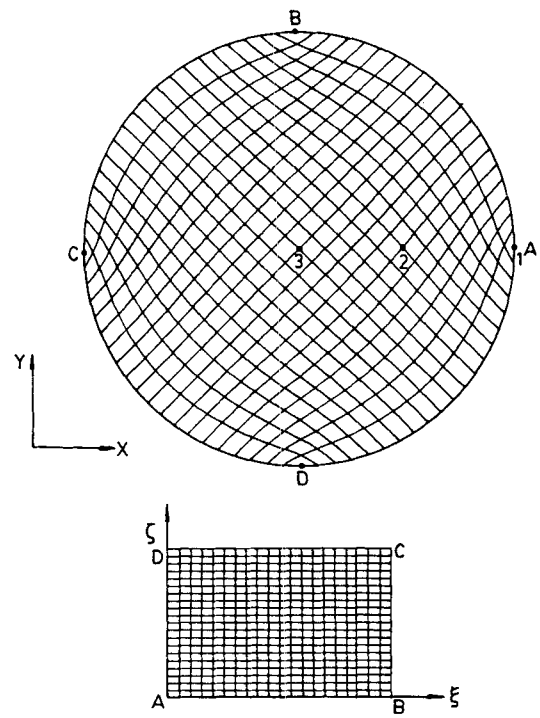

Figure 3. Grid B2 with $P=Q=0$ for the BFCTM

fluids with $n<1$, in agreement with previous observations.[22] We had no difficulty in convergence to $n=0{\cdot}1$ for the two grids. For the BFCTM the numerical mapping generally requires 40–50 iterations. We found that the proper estimation of the viscosity on the duct boundary is a critical factor for the convergence of the numerical procedure. Wheeler and Wissler[6] used the values of η at the neighbouring interior points to obtain η on the boundary through extrapolation. We found the ranges of convergence were limited with this approach; using the values of w to approximate shear rates and then evaluating η on the boundary appears to be a much better method. Clearly we could not use centred difference formulae to approximate shear rates on the boundary and (29) was used instead. Convergent solutions could also be obtained for n as small as 0·1.

A comparison of λ for various grids is shown in Table I. The errors increase slightly as n decreases for both methods. Using the 3×3 Gauss points for numerical integration is more accurate than using the 2×2 Gauss points, but the improvement is small. For the BFCTM the errors for grid B1 are relatively large compared with those for the other two refined grids, which generate quite accurate numerical solutions.

With the convergent solution of w available, we can estimate shear rates and viscosities. For the FEM we can use (18) to obtain these values at each nodal point within an element. If a node appears in several elements, we take the average value. We found that both the shear rates and viscosities estimated are extremely erroneous. This is understandable because the nine-node element we used belongs to the C^0-class elements.[15] For the BFCTM the estimation is straightforward; we can use (28), (29) to obtain the desired values.

Since grids F1 and B2 generate solutions of comparable accuracy, we shall compare the values of w on several points. The three points, which are indicated in Figure 2, were selected from grid B2 arbitrarily and grid F1 was then set up with these three points appearing as nodes. The results with $n=0{\cdot}5$ are shown in Table II. Since the values of the shear rates and viscosities computed are extremely erroneous for the FEM, they are not listed in the table. For these particular points selected, the velocities computed are accurate; the cases using the 2×2 Gauss points are slightly worse. For the BFCTM shear rates and viscosities can be approximated with reasonable accuracy. Since the power-law model is not valid at zero shear rate, point 3 is a singular point for viscosity estimation.

The CPU seconds consumed for grids F1 and B2 are given in Table III. For both methods we started the iteration with $n=1{\cdot}0$; the convergent solution with $n=0{\cdot}75$ was obtained and then used as the initial guess for the case $n=0{\cdot}5$. The FEM requires only 30% of the CPU time of the BFCTM to obtain numerical solutions of comparable accuracy.

Table I. Comparison of λ for the power-law model of a circular duct ($n=1{\cdot}0$, $\lambda^*_{ex}=6{\cdot}2832$; $n=0{\cdot}5$, $\lambda^*_{ex}=5{\cdot}0266$)

	FEM				BFCTM		
	Grid F1		Grid F2				
n	2×2 GP†	3×3 GP†	2×2 GP†	3×3 GP†	Grid B1	Grid B2	Grid B3
1·0	6·2953	6·2733	6·2816	6·2826	6·3840	6·3147	6·2980
err%†	0·38	0·16	0·026	0·0096	1·60	0·50	0·24
0·5	4·9972	5·0093	5·0221	5·0231	5·1275	5·0531	5·0455
err%‡	0·59	0·34	0·090	0·070	2·01	0·53	0·38

*ex = exact solution, †GP = Gauss points.
‡$\text{err}\% = (\lambda_{ex}-\lambda)/\lambda_{ex}\times100\%$.

Table II. Values of w, γ and η_P of the circular duct with $n=0.5$ (co-ordinates: point 1, $(x, y)=(2.0, 0.0)$; point 2, $(x, y)=(0.9644, -0.18\times10^{-5})$; point 3, $(x, y)=(0.12\times10^{-5}, 0.12\times10^{-5})$)

	Grid F1						Grid B2		
	2×2 GP			3×3 GP					
Point	1	2	3	1	2	3	1	2	3
w_{ex}	0	0·5919	0·6667	0	0·5919	0·6667	0	0·5919	0·6667
w^*_{num}	0	0·5842	0·6569	0	0·5910	0·6699	0	0·5933	0·6676
err%	0	1·30	1·46	0	0·16	0·49	0	0·24	0·13
γ_{ex}	—	—	—	—	—	—	1·0000	2·3251	7.3×10^{-12}
γ^*_{num}	—	—	—	—	—	—	1·0112	2·3713	6.8×10^{-6}
err%	—	—	—	—	—	—	1·12	1·99	—
$\eta_{P,ex}$	—	—	—	—	—	—	1·0000	2·0739	1.2×10^{6}
$\eta^*_{P,num}$	—	—	—	—	—	—	1·0148	2·0536	233·2
err%	—	—	—	—	—	—	1·48	0·99	—

*num = numerical solution.

Table III. CPU seconds consumed for the circular duct

Fluid model	FEM Grid F1 (3×3 GP)	BFCTM Grid B2
Power-law ($n=0.5$)	6.391	19·110 (3·497*)
Ellis ($\alpha=3$, $\tau_w/\tau_{1/2}=5$)	11·887	38·521 (3·497*)
Bingham ($\tau_w/\tau_0=5$)	3·910	17·253 (3·497*)

*CPU time required for mapping.

Since the exact solutions are not available for the other two duct geometries, we only present computed values of λ. For the FEM the grid for the equilateral triangular duct is shown in Figure 4 and consists of 12 elements and 61 nodes. A unit square, which was equally divided into 16 elements and 81 nodes, was used as the grid for the square duct. For the BFCTM a grid with 20×20 points was used for the equilateral triangular duct; this grid is shown in Figure 5. We also used a 20×20 grid with equal mesh intervals for the square duct. A comparison of λ for these two duct geometries is given in Table IV. The differences are very small for λ generated by these two methods. It is interesting to note that for the FEM there is no convergence problem with these two duct geometries; we could obtain solutions for n as small as 0·1. However, the BFCTM fails to converge if n is small. Table V lists the ranges of convergence for the three duct geometries. It is surprising that the ranges of convergence can be extended if we switch to equations (30), which use less points for approximation and are of first-order accuracy. Since for highly non-Newtonian fluid flow the shear rates vary rapidly near the duct boundary, so do the viscosities, and consequently using more points in the approximation does not necessarily give a closer estimation of the viscosities on the duct boundary.

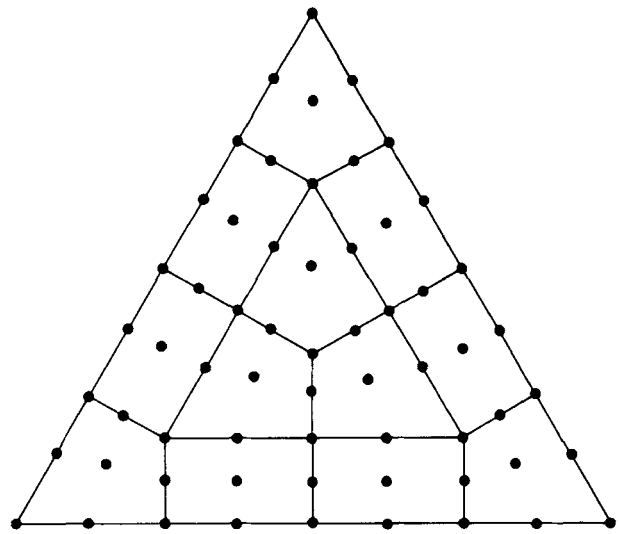

Figure 4. The FEM grid for the equilateral triangular duct

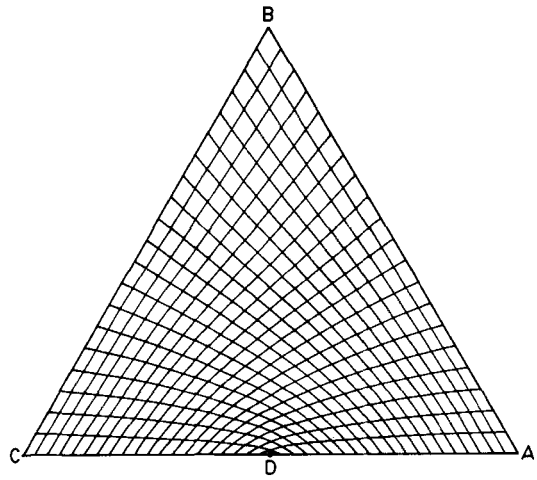

Figure 5. The 20×20 BFCTM grid with $P = Q = 0$ for the equilateral triangular duct

We have examined the effect of adjusting the relaxation factor on the range of convergence for power-law fluids. The triangular duct was tested and equations (29) were used to approximate shear rates. Several relaxation factors ranging from 0·75 to 1·85 were selected for the computation. It was found that the smallest value of n for which we could obtain convergent solutions was 0·4 for all the cases. Therefore adjusting the relaxation factor cannot extend the range of convergence. However, using a suitable relaxation factor, such as 1·75, needs much less CPU time for iteration than using other values.

Table IV. Comparison of λ for the triangular and square ducts

Fluid Model	Triangular duct			Square duct		
	FEM*	BFCTM	Diff†	FEM*	BECTM	Diff†
Power-law ($n=0{\cdot}5$)	11·451	11·563	0·98	7·817	7·769	0·60
Ellis ($\alpha=3$, $\tau_w/\tau_{1/2}=5$)	286·39	287·73	0·47	181·84	181·66	0·10
Bingham ($\tau_w/\tau_0=5$)	9·533	9·516	0·18	6·763	6·734	0·43

*Based on 3×3 GP.
†Diff $=|\lambda(\text{FEM})-\lambda(\text{BFCTM})|/\lambda(\text{FEM})\times100\%$.

Table V. The ranges of convergence for the BFCTM

	Circular duct*		Triangular duct*				Square duct*	
Power-law model								
n	0·1–1		0·4–1		0·2–1		0·3–1	0·1–1
P	0		0		0		0	0
Q	0		0		0		0	0
(29)	×		×				×	
(30)					×			×
Ellis model								
α	2	3	2	3	3	3	2	3
$\tau_w/\tau_{1/2}$	0–100	0–100	0–100	0–4	0–10	0–100	0–100	0–100
P	0	0	0	0	0·02	0	0	0
Q	0	0	0	0	−0·02	0	0	0
(29)	×	×	×	×	×		×	×
(30)						×		
Bingham model								
τ_w/τ_0	1–100		30–100	4–100	30–100	1–100		1–100
P	0		0	0·02	0	0·02		0
Q	0		0	−0·02	0	−0·02		0
(29)	×		×	×	×			×
(30)						×		

*The results are based on 20×20 grids for all three duct geometries.

The Ellis model

We need to specify two variables, α and $\tau_w/\tau_{1/2}$, in our computation. For the FEM we had no difficulty with convergence; however, the accuracy of the numerical solutions deteriorates as α or $\tau_w/\tau_{1/2}$ increases. Figure 6 shows the 1% accuracy curves for grids F1 and F2. The values of λ generated are within 1% error below the curves. It is observed from these two curves that if the

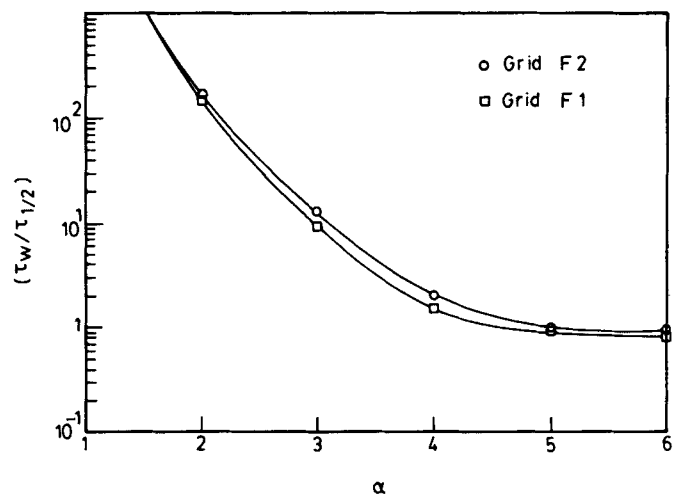

Figure 6. The 1% accuracy curves of λ based on the FEM for the Ellis model

element number is sufficiently large, such as in the case of grid F1, refining the mesh will not improve the numerical accuracy significantly. For the BFCTM the solution accuracy and the convergence behaviour are quite different. Figure 7 indicates the maximum values of $\tau_w/\tau_{1/2}$ for us to obtain convergent solutions using grid B2. If $\alpha < 3$, we can obtain accurate values of λ which are independent of $\tau_w/\tau_{1/2}$. As α increases, which implies the fluid becomes highly shear-thinning, both the ranges of convergence and the numerical accuracy decrease. A comparison of these two methods in terms of λ, w, γ and η_E is given in Table VI for $\alpha = 3$, $\tau_w/\tau_{1/2} = 5$. Both methods generate accurate values of λ. The estimations of γ and η_E are also extremely erroneous for the FEM and the results are not shown in the table. The errors in γ and η_E computed using the BFCTM are less

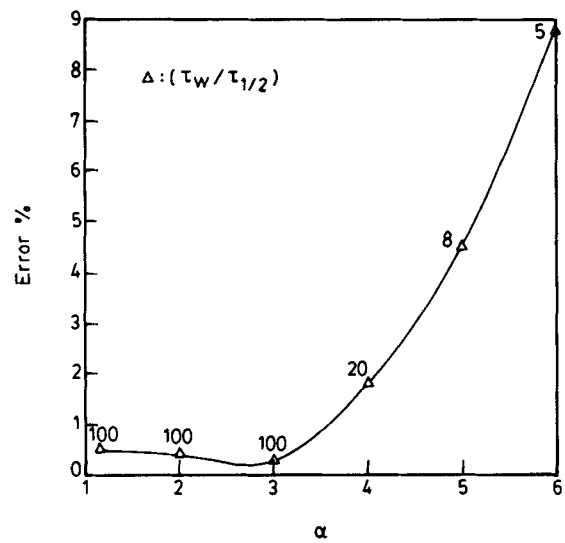

Figure 7. The ranges of convergence and computational accuracy of λ based on the BFCTM for the Ellis model

Table VI. Numerical results for the Ellis model with $\alpha=3$, $\tau_w/\tau_{1/2}=5$ ($\lambda_{ex}=111{\cdot}0$; λ(grid F1)$=110{\cdot}06$, err%$=0{\cdot}85$; λ(grid B2)$=110{\cdot}82$, err%$=0{\cdot}17$)

	Grid F1 (3 × 3 GP)			Grid B2		
Point	1	2	3	1	2	3
w_{ex}	0	12·592	13·500	0	12·592	13·500
w_{num}	0	12·559	13·553	0	12·576	13·500
err%	0	0·26	0·39	0	0·13	0·001
γ_{ex}	—	—	—	26·000	3·285	0
γ_{num}	—	—	—	24·690	3·431	0
err%	—	—	—	5·04	4·44	0
$\eta_{E,ex}$	—	—	—	0·0385	0·147	1·000
$\eta_{E,num}$	—	—	—	0·0404	0·143	1·000
err%	—	—	—	4·99	2·70	$1{\cdot}0\times10^{-6}$

than 5%. The CPU seconds consumed are also given in Table III. For both methods we started the iteration with the Newtonian case and the solution was used as the initial guess for the case $\alpha=3$, $\tau_w/\tau_{1/2}=5$. Since η_E has to be determined iteratively at each Gauss point, more CPU time is required for obtaining convergent solutions. Again the FEM consumes much less CPU time than the BFCTM.

Values of λ for the other two geometries are also given in Table IV. We used the same grids as for the power-law model and the differences are small. For the FEM there is no convergence problem with these two duct geometries. For the BFCTM the ranges of convergence for $\alpha=2$ and 3 are also indicated in Table V. The equilateral triangular duct seems to be an awkward geometry for the BFCTM. However, we can either use (30) or adjust P and Q to improve the convergence. It is noted that with minor adjustments of P and Q we can expand the ranges of convergence significantly. A modified grid with non-zero P and Q for the equilateral triangular duct is shown in Figure 8.

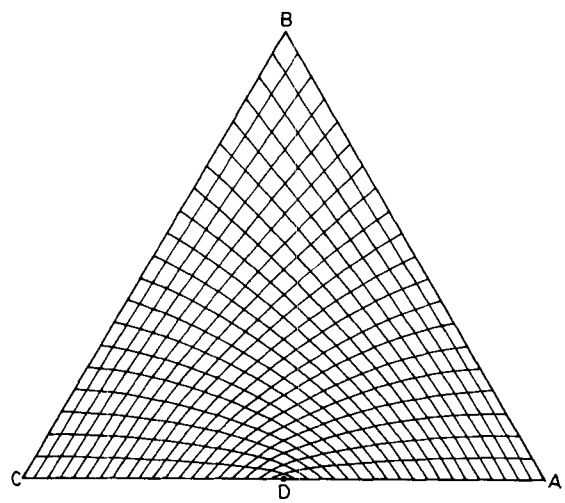

Figure 8. The 20 × 20 BFCTM grid with $P=0{\cdot}02$, $Q=-0{\cdot}02$ for the equilateral triangular duct

The Bingham model

The numerical accuracy deteriorates as τ_w/τ_0 decreases; there will be no flow if $\tau_w/\tau_0 = 1$. The errors in λ are around 1% for grids F1 and B2 with $\tau_w/\tau_0 = 2$. Values of λ, w, γ and η_B are shown in Table VII for the circular duct. Similarly both methods generate accurate λ and w, but γ and η_B can only be approximated with reasonable accuracy using the BFCTM. The CPU time used is also given in Table III. The Newtonian solution was again used as the initial guess. The FEM consumes much less CPU time as in the previous cases. Values of λ for the other two duct geometries are also given in Table IV. The same grids were used and the differences are again small.

There is no convergence problem for the FEM. For the BFCTM the convergence difficulty arises if τ_w/τ_0 is close to one for the equilateral triangular duct. Again we need to adjust P and Q or use (30). The ranges of convergence are also indicated in Table V.

CONCLUSIONS

We have analysed inelastic non-Newtonian fluid flow in ducts of irregular cross-section. The fluids under consideration belong to the class of generalized Newtonian fluids (GNF). We have found both the Galerkin finite element method and the boundary-fitted co-ordinate transformation method can be used to solve the flow problem.

Three representative GNF models, namely the power-law, the Ellis and the Bingham models, have been studied in detail. Both methods can generate solutions of high accuracy for practical ranges of variables. As the fluid becomes highly non-Newtonian, i.e. the fluid is highly shear-thinning or its yield stress is relatively important, the numerical accuracy deteriorates for both methods.

For the three duct geometries we studied, the FEM does not have any convergence problems. However, we found for the BFCTM that using appropriate one-sided formulae to compute viscosities on the duct boundary is a critical factor for generating convergent solutions. The equilateral triangular duct is particularly awkward for our computation; proper adjustments of the forcing functions P and Q are also necessary for us to obtain convergent solutions.

For the FEM we approximated the shear rates and viscosities on the nodal point by averaging those values obtained from each element in which the particular node was included. With this

Table VII. Numerical results for the Bingham model with $\tau_w/\tau_0 = 5$ ($\lambda_{ex} = 4{\cdot}611$; λ(grid F1) $= 4{\cdot}605$, err% $= 0{\cdot}14$; λ(grid B2) $= 4{\cdot}638$, err% $= 0{\cdot}58$)

	Grid F1 (3 × 3 GP)			Grid B2		
Point	1	2	3	1	2	3
w_{ex}	0	0·560	0·640	0	0·560	0·640
w_{num}	0	0·561	0·655	0	0·562	0·637
err%	0	0·13	2·41	0	0·21	0·40
γ_{ex}	—	—	—	0·800	0·282	0
γ_{num}	—	—	—	0·834	0·283	0
err%	—	—	—	4·24	0·39	0
$\eta_{B,ex}$	—	—	—	1·250	1·709	1·000
$\eta_{B,num}$	—	—	—	1·251	1·706	1·000
err%	—	—	—	0·10	0·16	0

approach we found the values obtained are extremely erroneous. As one of the reviewers suggested, it is possible to deduce viscosities at nodes more accurately if they are evaluated at the Gauss points and then interpolated onto the finite element trial functions. For the BFCTM we could estimate the shear rates and viscosities on each grid point easily and the results are reasonably accurate. For all the cases we have studied, the solution generated by the FEM requires only 30% of the CPU time of that generated by the BFCTM for the same level of accuracy.

ACKNOWLEDGEMENT

This research was supported by the National Science Council, Republic of China.

NOTATION

A	variable; equation (21)
a, b, c	variables; equation (24c)
$\bar{D}, D$	cross-sectional area of the duct, dimensional and dimensionless
∂D	boundary of D
f	a general function; equations (28)–(30)
h	characteristic length
J	Jacobian; equation (24c)
k, n	material constants of the power-law model
K	variable; equation (20)
L	number of nodes in an element
M, N	numbers of grid points for the BFCTM
$\bar{P}$	pressure
P, Q	forcing functions; equations (24a) and (24b)
r, s	mesh intervals of the BFCTM
S	wetted perimeter
$\bar{V}$	volumetric flow rate
$\bar{w}, w$	axial velocity component, dimensional and dimensionless
$(\bar{x}, \bar{y}, \bar{z})$	Cartesian co-ordinates
(x, y)	lateral Cartesian co-ordinates, dimensionless

Greek letters

$\alpha, \tau_{1/2}$	material constants of the Ellis model
β	variable; equation (22)
γ	shear rate
γ_c	critical shear rate for the Bingham model
δ	variable; equation (19)
$\mathbf{\Delta}$	rate of deformation tensor
η	apparent viscosity
η_0	reference viscosity
λ	dimensionless volumetric flow rate
(ξ, ζ)	mapped co-ordinates for the BFCTM
$\boldsymbol{\tau}, \bar{\tau}$	stress tensor and its magnitude
τ_0	yield stress
τ_w	average wall stress

$\bar{\tau}_{xz}, \bar{\tau}_{yz}$ components of $\boldsymbol{\tau}$
ϕ interpolation function

Subscripts

i, j, m indices
P the power-law model
E the Ellis model
B the Bingham model

REFERENCES

1. C. Miller, 'Predicting non-Newtonian behavior in ducts of unusual cross-section', *Indust. Eng. Chem. Fund.*, **11**, 524–528 (1972).
2. R. S. Schechter, 'On the steady flow of a non-Newtonian fluid in cylinder ducts', *AIChE J.*, **7**, 445–448 (1961).
3. T. Mizushima, N. Mitsuishi and R. Nakamura, 'On the flow of power model fluid in elliptic tube', *Kagaku Kogaku*, **28**, 648–654 (1965).
4. N. Mitsuishi, Y. Kitayama and Y. Aoyagi, 'Non-Newtonian flow in non-circular ducts', *Int. Chem. Eng.*, **8**, 168–174 (1968).
5. R. L. Batra and K. Koshy, 'Flow of Casson fluids in non-circular ducts', *Biorheol.*, **15**, 15–27 (1978).
6. J. A. Wheeler and E. H. Wissler, 'The friction factor–Reynolds number relation for the steady flow of pseudoplastic fluids through rectangular ducts', *AIChE J.*, **11**, 207–216 (1965).
7. T. J. Liu, 'Fully developed flow of power-law fluids in ducts', *Indust. Eng. Chem. Fund.*, **22**, 183–186 (1983).
8. W. Kozicki, C. H. Chou and C. Tiu, 'Non-Newtonian flow in ducts of arbitrary cross-sectional shape', *Chem. Eng. Sci.*, **21**, 665–679 (1966).
9. R. W. Hanks, 'On the prediction of non-Newtonian flow behavior in ducts of noncircular cross section', *Indust. Eng. Chem. Fund.*, **13**, 62–66 (1974).
10. T. J. Liu and C. N. Hong, 'The pressure drop/flow rate equation for non-Newtonian flow in channels of irregular cross-section', *Polym. Eng. Sci.*, (1987) in press.
11. R. B. Bird, R. C. Armstrong and O. Hassager, *Dynamics of Polymeric Liquids, Vol.* 1, Wiley, New York, 1977.
12. P. S. Huyakorn, C. Taylor, R. L. Lee and P. M. Gresho, 'A comparison of various mixed-interpolation finite elements in the velocity–pressure formulation of the Navier–Stokes equations', *Comput. Fluids*, **6**, 25–36 (1978).
13. P. W. Chang, T. W. Patten and B. A. Finlayson, 'Collocation and Galerkin finite-element method for viscoelastic fluid flow', *Comput. Fluids*, **7**, 267–283 (1979).
14. T. J. Liu, 'An efficient matrix solver for finite-element analysis of non-Newtonian fluid flow problems', *Int. j. numer. methods fluids*, **5**, 929–938 (1985).
15. O. C. Zienkiewicz, *The Finite-Element Method*, McGraw-Hill, London, 1977.
16. T. J. Chung, *Finite-Element Analysis in Fluid Dynamics*, McGraw-Hill, New York, 1978.
17. J. F. Lyness, D. R. J. Owen and O. C. Zienkiewicz, 'Finite-element analysis of non-Newtonian fluids through parallel-sided conduits', in J. T. Oden, O. C. Zienkiewicz, R. H. Gallagher and C. Taylor (eds), *Finite-Element Method in Flow Problems*, University of Alabama Press, Huntsville, 1979, pp. 489–501.
18. P. Hood, 'Frontal solution program for unsymmetric matrices', *Int. j. numer. methods eng.*, **10**, 379–400 (1976).
19. E. J. O'Donovan and R. I. Tanner, 'Numerical study of the Bingham squeeze film problem', *J. Non-Newtonian Fluid Mech.*, **15**, 75–83 (1984).
20. J. F. Thompson, Z. U. A. Warsi and C. W. Mastin, 'Boundary-fitted coordinate systems for numerical solution of partial differential equations—a review', *J. Comput. Phys.*, **47**, 1–108 (1982).
21. J. F. Thompson, F. C. Thames and C. W. Mastin, 'Automatic numerical generation of body-fitted curvilinear coordinate system for field containing any number of arbitrary two-dimensional bodies', *J. Comput. Phys.*, **15**, 299–319 (1974).
22. D. K. Gartling, 'Finite element methods for non-Newtonian flows', *Tech. Rep. SAND85-1704*, Sandia National Laboratories, Albuqerque, New Mexico, 1986.